Reducing Lattice Thermal Conductivity of MnTe by Se Alloying toward High Thermoelectric Performance

Jinfeng Dong,[†] Fu-Hua Sun,[†] Huaichao Tang,[†] Kei Hayashi,[‡] Hezhang Li,[‡] Peng-Peng Shang,[†,§] Yuzuru Miyazaki,[‡] and Jing-Feng Li*[,†]

[†]State Key Laboratory of New Ceramics and Fine Processing, School of Materials Science and Engineering, Tsinghua University, Beijing 100084, China

[‡]Departmant of Applied Physics, Graduate School of Engineering, Tohoku University, Sendai 980-8579, Japan

[§]College of Chemistry and Materials Science, Shandong Agricultural University, Taian 271018, China

S *Supporting Information*
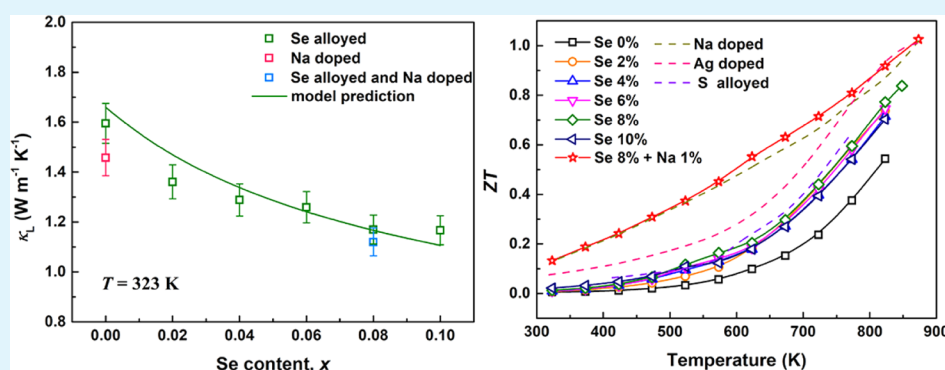
ABSTRACT: Lead-free manganese telluride has been considered to be a promising candidate for mid-temperature thermoelectric materials. In this work, we report point defect scattering-induced reduction of thermal conductivity in MnTe with Se alloying, fabricated by a facile method combining mechanical alloying and spark plasma sintering. A low lattice thermal conductivity of 0.56 W/mK was obtained for $MnTe_{0.92}Se_{0.08}$, which is quite close to the amorphous limits. A detailed Debye model analysis reveals the underlying mechanism of phonon scattering and well predicts the thermal conductivity with different contents of Se. Meanwhile, a slight increase of carrier concentration was also observed after Se alloying, accompanied by a variation of energy gap that may be associated with the competition among anions in trapping charges. Further Na doping leads to enhanced electrical transport properties, achieving a maximum ZT value of 1.03 at 873 K. An average ZT of 0.52 and a calculated efficiency of more than 9% also suggest the promising application of MnTe at medium temperatures.

KEYWORDS: manganese telluride, thermoelectric, Se alloying, thermal conductivity, Debye model

INTRODUCTION

Thermoelectric materials can realize the direct conversion of heat and electricity,[1] whose efficiency is quantified by the dimensionless figure of merit $ZT = S^2T/\rho\kappa$, where S, ρ, κ, and T denote the Seebeck coefficient, electrical resistivity, thermal conductivity, and absolute temperature, respectively.[2−5] Notably, two distinctive strategies could be proposed to enhance the thermoelectric performance: one is to optimize the power factor[6,7] $(PF = S^2/\rho)$ via modulation of carrier concentration[8] and band structure[9] and the other one is to decrease κ through introduction of different dimension of defects like point defects,[10,11] dislocations,[12−14] grain boundaries,[15] and nanoinclusions.[16,17]

To realize the recovery of waste heat, developing a high-performance thermoelectric material working at medium temperatures has drawn considerable attention. Manganese tellurite (MnTe) with an indirect band gap of 0.86 eV[18] has

been investigated as a promising thermoelectric material recently. In 2013, Kim et al. successfully synthesized pristine MnTe by the melt-quench process and reported a high ZT of 0.41 at 773 K.[19] Subsequently, pristine MnTe was also fabricated through mechanical alloying (MA)[20] and combustion synthesis,[21] verifying its potential application as a thermoelectric material as well. To improve the poor electrical transport properties caused by the low carrier concentration of pristine MnTe, a lot of dopant elements on the Mn site have been reported including alkaline metals,[22,23] copper,[24] and silver.[25] The carrier concentration of MnTe has been increased to a level of $\sim10^{20}$ cm^{-3}, and an enhanced power factor over 800 μW/mK^2 has been achieved.

Although ZT values of MnTe have been much improved by optimizing PF, there is still room for improvement if thermal conductivity could be much decreased, which is widely considered as the most effective strategy to enhance the thermoelectric performance.[26,27] For pristine MnTe, the lattice thermal conductivity is commonly 0.66 W/mK at 873 K and more than 1.2 W/mK at 323 K,[19−21] which is still much higher than the minimum lattice thermal conductivity.[25] Moreover, among all kinds of defects, point defect is effective in suppressing the propagation of phonons for its small dimension to scatter the high-frequency phonons.[28] MnX (X = S, Se, and Te), the so-called crossroads materials,[29] possess a similar crystal structure as NiAs and thus may guarantee a high solid solubility with each other, supplying sufficient point defects to decrease the thermal conductivity.

Herein, we synthesized high-quality, Se-alloyed MnTe to investigate the effects of point defects on thermal conductivity and ZT values. The thermal conductivity was largely suppressed from 1.6 to 1.1 W/mK at 323 K and decreased to 0.58 W/mK at 823 K, which is close to the minimum lattice thermal conductivity. Taking into consideration the effects of point defects introduced by Se ions, a thorough analysis of the Debye−Callaway model reasonably explained the reduction of thermal conductivity. Furthermore, Se alloying was found to simultaneously realize a narrower band gap of MnTe and slightly increase the carrier concentration as well as power factor. Combining the optimized thermal conductivity and enhanced PF, a high ZT of 0.82 was realized in $MnTe_{0.92}Se_{0.08}$. Additionally, Na doping further elevated the ZT value to 1.03 at 823 K, achieving high efficiency and average ZT. The low thermal conductivity and high ZT reveal the effectiveness of Se alloying-induced point defects in MnTe.

■ EXPERIMENTAL SECTION

Mn (pieces, 99.9%), Te (powders, 99.999%), Se (powders, 99.9%), and Na_2Te (powders, 99.9%) were weighted according to the stoichiometry $MnTe_{1−x}Se_x$ or $Na_{0.01}Mn_{0.99}Te_{0.92}Se_{0.08}$ and then subject to mechanical alloying (MA) using a planetary ball mill at 450 rpm for 12 h. An extra 1.5% manganese was added to compensate for the possible oxidation of the raw material. A jar made of tungsten carbide were applied, and Ar was used as the protective gas. The ball-milled powders were consolidated by spark plasma sintering (SPS 211Lx, Fuji Electronic Industrial Co., Ltd., Japan) at 973 K for 5 min under an axial pressure of 60 MPa.

The phase structure was evaluated by X-ray diffraction (D8 Advance, Bruker, Germany, Cu Kα). The morphology and micro-structure of sintered samples were confirmed by a field-emission scanning electron microscope (SEM, Zeiss Merlin, Germany) and a transmission electron microscope (TEM, JEOL JEM-2100F). A UV−vis−NIR spectrum system (Cary 5000, Varian) was used to collect optical absorption spectra. The Seebeck coefficient (S) and electrical resistivity (ρ) were measured by a Seebeck coefficient/electric resistance measuring system (ZEM-2, Ulvac-Riko, Japan). The total thermal conductivity was calculated via the equation $\kappa = DC_pd$, where D represents the thermal diffusivity determined by the laser flash diffusivity method (Netzsch, LFA 457, Germany), d is the density measured by the Archimedes method, and C_p is the specific heat.[20] The Hall coefficient (R_H) was measured under a reversible magnetic field of 0.52 T (ResiTest 8340DC, Toyo, Japan), and the Hall carrier concentration and mobility were calculated by $n_H = 1/(eR_H)$ and $\mu_H = R_H/\rho$, respectively. Longitudinal and transverse sound velocities (v_l and v_t) were measured by the ultrasonic pulse-echo technique (5072PR, Olympus, Tokyo, Japan).

■ RESULTS AND DISCUSSION

Figure 1a presents the X-ray powder diffraction (XRD) patterns of $MnTe_{1−x}Se_x$. The high phase purity was confirmed
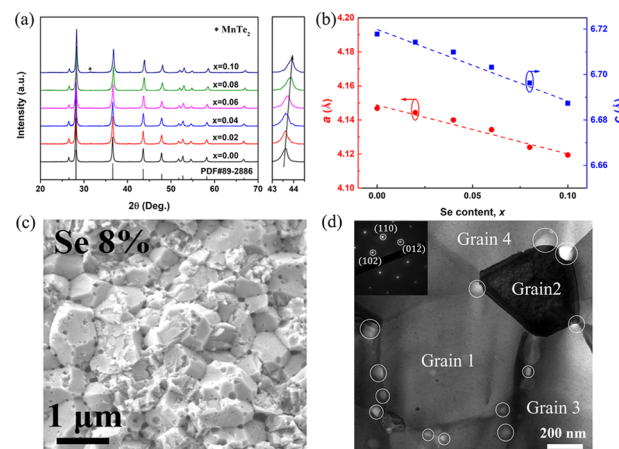

Figure 1. (a) XRD patterns of bulk samples for $MnTe_{1−x}Se_x$, along with the enlarged peaks between 43 and 44°. (b) Calculated lattice parameters as a function of Se content. (c) SEM image on the fracture surface of 8% Se-alloyed MnTe. (d) Bright-field TEM image of $MnTe_{0.92}Se_{0.08}$ with white circles indicating the small pores; the inset figure is the selected-area electron diffraction (SAED) pattern showing the hexagonal structure of MnTe.

as all of the peaks are indexed to the standard PDF card (#89-2886) except for a small amount of $MnTe_2$ found in $MnTe_{0.9}Se_{0.1}$. The enlarged peak at around 43° shows a clear shift toward higher angles for the smaller ionic radius of $Se^{2−}$ than $Te^{2−}$.[30] The calculated parameters a and c, as shown in Figure 1b, also decrease linearly with the increase of alloying Se contents, further verifying the substitution of $Te^{2−}$ by $Se^{2−}$. Homogeneously distributed elements (Mn, Te, and Se) are confirmed in Figure S2 with the energy dispersive X-ray spectrometry (EDS) mapping image on the polished surface of $MnTe_{0.92}Se_{0.08}$ at a scale of several micrometers, showing the high quality of synthesized samples. The phase structure analysis above surely indicates the successful formation of $MnTe_{1−x}Se_x$ solid solutions.

The morphology of Se-alloyed MnTe in Figure 1c shows an average grain size of 1 μm and fruitful small pores around the surface of the grain, which have no detectable difference compared to the pristine ones.[20] The nanopores, which distribute around the grain boundaries between several grains, were also detected in the TEM image, as shown in Figure 1d, which was according to the SEM image. The formation of plentiful nanopores may be due to the fast densification of SPS and volatilization of Te and Se. The pores in the nanoscale dimension are believed to act as scattering centers to suppress the propagation of phonons. Moreover, elements are still distributed homogeneously at the nanoscale except for a little segregation of Mn in grain boundaries, as shown in Figure S3. The selected-area electron diffraction (SAED) pattern also indicates the hexagonal nature of MnTe.

The electrical transport properties of $MnTe_{1−x}Se_x$ are measured and presented in Figure 2. As the alloying content of Se increases, the electrical resistivity as well as the Seebeck coefficient slightly decreases at 323 K, according to the enhancement of carrier concentration, as shown in Figure 2c. The rapid decrease of S and ρ at elevated temperatures is
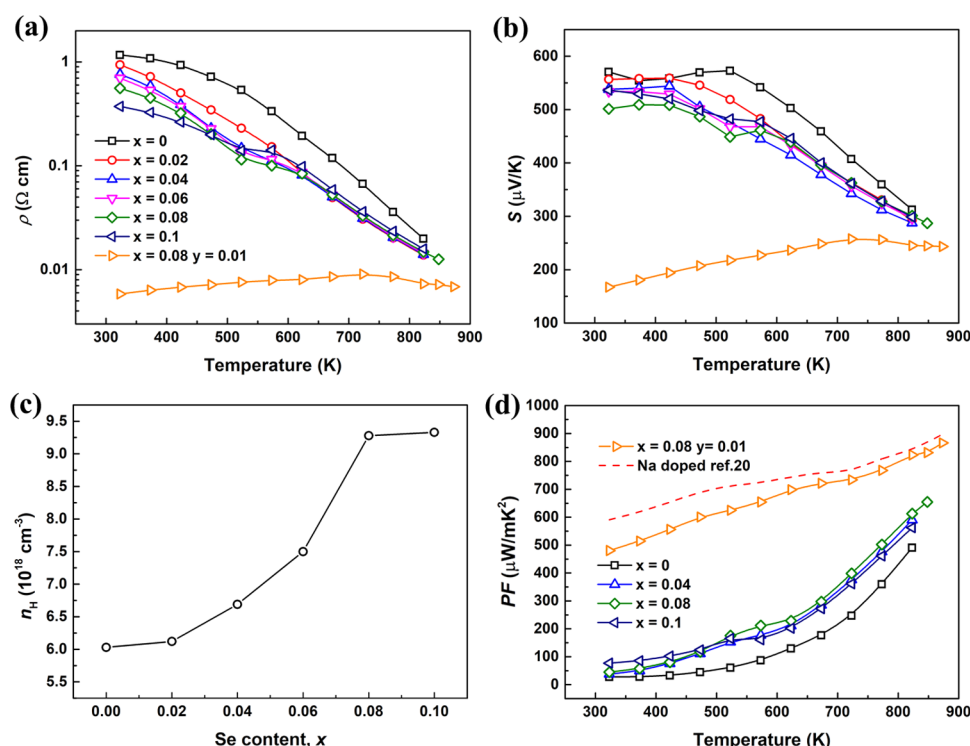
Figure 2. (a) Electrical resistivity, (b) Seebeck coefficient, and (d) PF of $MnTe_{1-x}Se_x$ and Na-doped samples as a function of temperature. (c) Se content dependence of carrier concentration.

related to the intrinsic excitation, and the abnormal inflection at around 500 K should be ascribed to some thermally activated defects (more analysis can be found in the Supporting Information (SI)). Thanks to the increased carrier concentration from 6×10^{18} cm^{-3} to more than 9×10^{18} cm^{-3} after Se alloying, an enhancement of PF was achieved especially in $MnTe_{0.92}Se_{0.08}$ when compared to that of the pristine MnTe. Furthermore, the improvement of electrical transport property was realized by doping with Na, which was proved to be an efficient hole dopant and a little substitution of Mn such as 1% could largely increase the electrical conductivity.[20,23] The electrical resistivity decreases drastically from ~1 to 0.006 Ω cm, accompanied by a decrease of the Seebeck coefficient, as shown in Figure 2a,d, which is due to the drastic elevation of hole carrier concentration shown in Figure S4. Although such an enhanced hole carrier concentration is comparable to those reported in sodium-doped samples,[20,23] the PF is inferior to that obtained in only Na-doped MnTe especially at a relatively low temperature, which is mainly due to carrier scattering from the alloyed Se ion.

To investigate the underlying mechanism for the increased carrier concentration induced by the isoelectronic dopants of Se, the band gaps (E_g) of $MnTe_{1-x}Se_x$ were examined. The E_g calculated through the Arrhenius method,[20,29] presented in Figure 3, shows a decreased tendency as the content of Se increases, which was in line with a red shift upon Se substitution demonstrated in the inset figure. A simple schematic illustration of such a variation of band gap is shown in Figure S5. A similar effect was also observed in sulfur-substituted MnTe,[29] which is hard to understand at the first glance as MnSe (or MnS) holds a larger band gap than MnTe.[31]
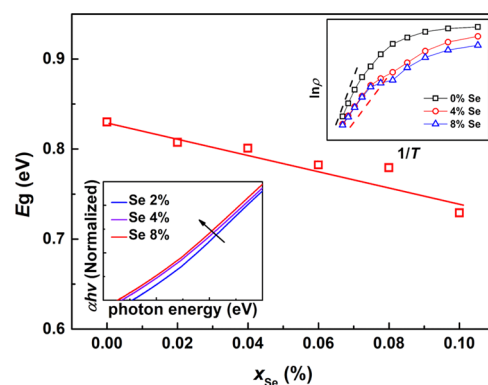
Figure 3. Se content-dependent energy gap of $MnTe_{1-x}Se_x$ calculated by the Arrhenius simulation; the inset figure shows the $\ln\rho$ vs $1/T$ plot and the results of optical absorption spectra.

Actually, such a nonlinear dependence of the band gap with the alloy composition was called the band gap bowing character, which is usually observed in transition metal chalcogenides such as $CdSe_xTe_{1-x}$ and may be connected to the competition among anions (Se and Te) in trapping charges.[32] Although the above analysis gives one possible explanation, a more detailed investigation from the perspective of theoretical calculation is needed to fully explain the phenomenon.

The total thermal conductivity and lattice thermal conductivity are shown as a function of temperature in Figures 4a and S6. The decrease of total and lattice thermal conductivities with temperature indicates the strengthened Umklapp scattering of phonon, while the monotonous reduction of lattice thermal conductivity with the Se content suggests the enhanced alloying scattering of phonon. For $MnTe_{0.92}Se_{0.08}$, rather low κ_L values of ~1.1 and ~0.56 W/mK
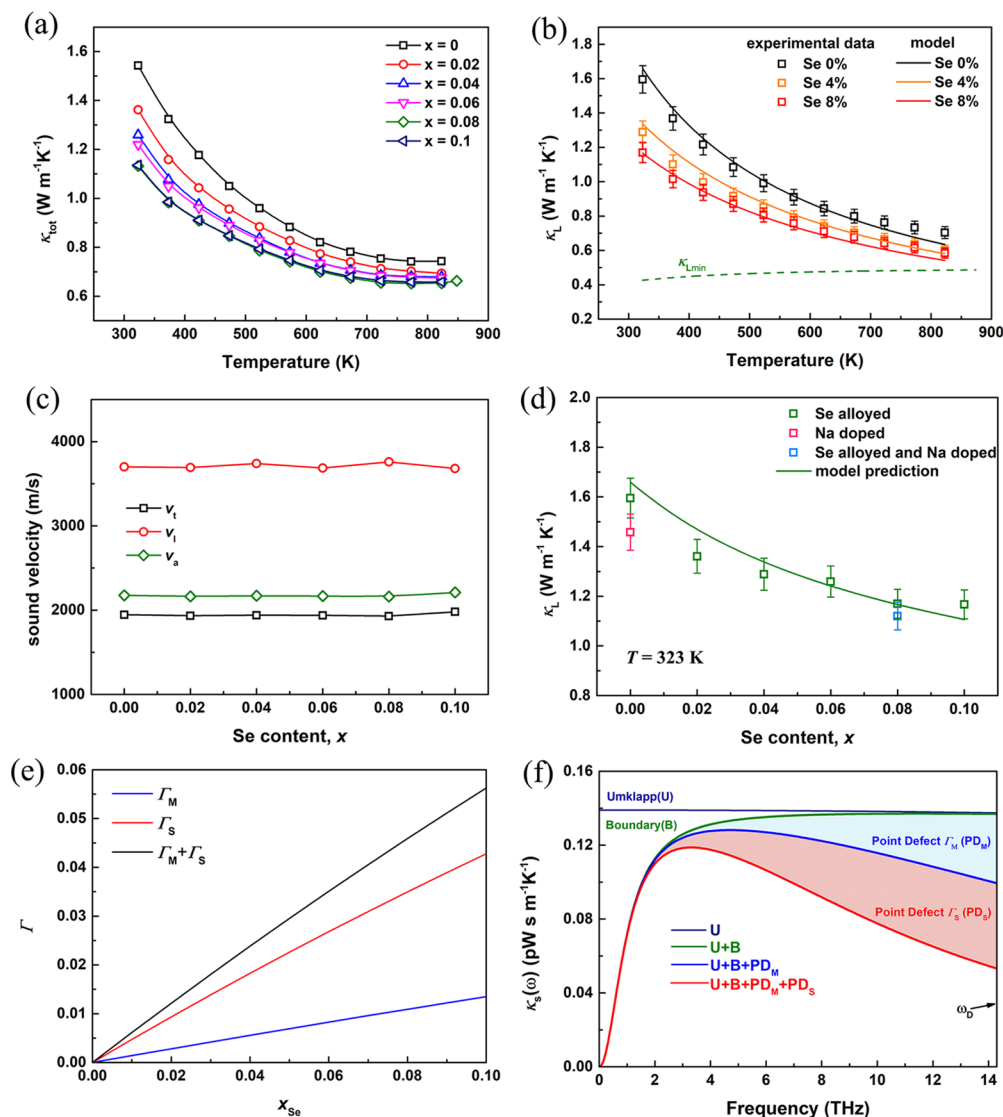
Figure 4. (a) Total thermal conductivity of Se-alloyed MnTe. (b) Corrected lattice thermal conductivity of MnTe$_{1-x}$Se$_x$ and results of Debye model simulation; an amorphous limit of lattice thermal conductivity is also shown as a dashed line. (c) Longitudinal and traverse sound velocity of MnTe$_{1-x}$Se$_x$. (d) Se content dependence of lattice thermal conductivity and Debye simulation results at 323 K; a reference of thermal conductivity of Na doped without Se alloying is included.[20] (e) Calculated values of mass, strain, and total fluctuation parameters. (f) Frequency-dependent lattice thermal conductivity.

were obtained at 323 and 850 K, respectively. The low thermal conductivity at 850 K is quite close to the amorphous limit of κ_L (κ_{Lmin}), which was calculated using the model of Cahill et al.[33]

$$\kappa_{Lmin} = \left(\frac{\pi}{6}\right)^{1/3} k_B n^{2/3} \sum_i v_i \left(\frac{T}{\theta_i}\right) \int_0^{\theta_i/T} \frac{x^3 e^x}{(e^x - 1)^2} dx \quad (1)$$

where the sum is over the three sound modes with speeds of v_i, n represents the number density of atoms, and the cutoff frequency (θ_i) was determined as $\theta_i = v_i (h/k_B)(3n/4\pi)^{1/3}$. The significant reduction of thermal conductivity further demonstrates the effectiveness of alloying scattering introduced by Se substitution.

To understand the reduction of thermal conductivity with Se alloying, the Debye model was applied. The lattice thermal conductivity of samples with different Se contents was first rectified to full dense values to eliminate the influence of

porosity using the following equation and is shown in Figure 4b,d.

$$\frac{\kappa_{real}}{\kappa_{dense}} = 1 - \frac{4}{3}\phi \quad (2)$$

where κ_{real}, κ_{dense}, and ϕ denote the measured thermal conductivity, full dense values, and porosity, respectively.[34] Then, the Debye model explains the lattice thermal conductivity as a summation of phonons with different frequencies via[35,36]

$$\kappa_L = \frac{k_B}{2\pi^2 v_a} \left(\frac{2\pi k_B T}{h}\right)^3 \int_0^{\theta_a/T} \tau(x) \frac{e^x x^4}{(e^x - 1)^2} dx \quad (3)$$

where v_a is the average sound velocity calculated by $v_a^{-3} = (2v_t^{-3} + v_l^{-3})/3$, θ_a is the average acoustic Debye temperature derived from the Debye temperature (Θ) through $\theta_a = \Theta/n^{1/3}$ (here, $n = 4$ for MnTe is the atomic number per primitive unit cell), $x = \hbar\omega/k_B T$ is the reduced phonon energy, and $\tau(x)$ is
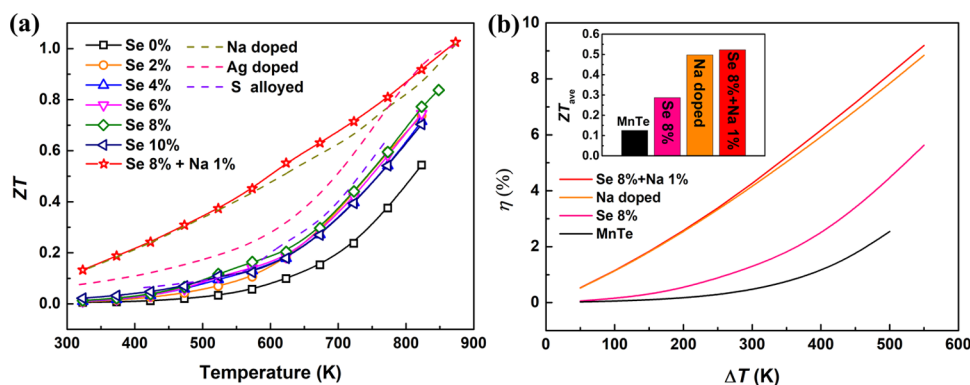
Figure 5. (a) Temperature-dependent *ZT* values of Se-alloyed and/or Na-doped MnTe including some reported data.[20,25,29] (b) Calculated conversion efficiency as a function of temperature difference; the inset figure shows the average *ZT* values; the cold temperature is fixed at 323 K.

the total relaxation time. The Se content-dependent sound velocity, which is shown in Figure 4c, exhibits a nearly same value. The unchanged v_t and v_l mean the Debye temperature and phonon dispersion are not varied much in up to 10% Se-alloyed MnTe, also demonstrating the effectiveness of the Debye model. The detailed calculation of Debye temperature and total relaxing time is listed in the SI.

Simulation results as a function of temperature and Se content are shown in Figure 4b,d, respectively. It could be seen that the model simulated the experimental data quite well and the discrepancy at high temperatures could be ascribed to the contributions from bipolar diffusion. It is also clearly seen that the model well predicts the reduction of lattice thermal conductivity induced by point defect scattering of Se atoms and a significant decrease of more than 30% is attained at 323 K as x increases to 0.08. The quantities of Γ_M and Γ_S, which evaluate the intensity of the impact on lattice thermal conductivity, are shown in Figure 4e. With a larger value of Γ_S, the reduction of lattice thermal conductivity is more pronounced with strain fluctuation than mass fluctuation, resulted from the difference of ionic radius and mass between Se and Te ions. The frequency-dependent lattice thermal conductivity of dense Se-alloyed MnTe is shown in Figure 4f, which indicates that interfaces influence low-frequency phonons, while point defects scatter high-frequency phonons. The more significant scattering of phonons from point defects with Γ_S shown in Figure 4f is also according to the above analysis. Moreover, the lattice thermal conductivity of sodium and selenium codoped samples also agrees with the values calculated by models, verifying the effectiveness of the Debye model in explaining the thermal conductivity of MnTe. The significant role of Se could also be demonstrated from the much lowered lattice thermal conductivity of the sodium and selenium codoped sample when compared with that of the only sodium-doped sample, as shown in Figure 4d, indicating the benefit of selenium alloying to scatter the phonons and lead to the high thermoelectric performance.

Figure 5a shows the *ZT* values of MnTe$_{1-x}$Se$_x$, Na$_{0.01}$Mn$_{0.99}$Te$_{1-x}$Se$_x$, and some literature data as a function of temperature. The slightly improved electrical conductivity and the significant reduction of thermal conductivity promise the enhancement of *ZT* values for Se-substituted MnTe. A high *ZT* value of 0.84 is obtained in MnTe$_{0.92}$Se$_{0.08}$ at 850 K. Furthermore, additional sodium doping increases the *ZT* values to 1.03 at 873 K with an increase of average *ZT* (*ZT*$_{ave}$),

as shown in the inset pattern of Figure 5b, which is defined as follows.

$$ZT_{ave} = \frac{\int_{T_{cold}}^{T_{hot}} ZT(T)\, dT}{T_{hot} - T_{cold}} \qquad (4)$$

$$\eta = \frac{\Delta T}{T_{hot}} \frac{\sqrt{1 + ZT_{ave}} - 1}{\sqrt{1 + ZT_{ave}} + T_{cold}/T_{hot}} \qquad (5)$$

The high *ZT*$_{ave}$ guarantees the superior convention efficiency, and a maximum calculated efficiency of more than 9% is realized in Na$_{0.01}$Mn$_{0.99}$Te$_{0.92}$Se$_{0.08}$ at a temperature difference of 550 K. However, it should be noted that the influence of the guest atom on the mobility of carriers and also the reduced effectiveness of point defect scattering at high temperatures prevent the further enhancement of *ZT* values, so other methods such as different doping elements should be considered to tune the Fermi level while the mobility is not affected. Moreover, possible efforts such as nanostructure[3,37,38] and dense dislocation arrays[12−14] could also be desired to affect a broad range of phonons with different frequencies.

■ CONCLUSIONS

This work has investigated the thermoelectric properties of MnTe alloyed with different contents of Se. It is found that Se alloying could lead to a slight decrease of energy gap and thus increase the carrier concentration from 6×10^{18} to 9.5×10^{18} cm^{-3}, resulting in an enhanced *PF* by 30%. Further doping of sodium drastically decreased the electrical resistivity to 0.006 Ω cm at 323 K and increased the electrical transport properties. Point defect scattering induced by the guest atom of Se was proved to effectively suppress the propagation of high-frequency phonons, and a low lattice thermal conductivity of 0.56 W/mK was attained, which was close to the amorphous limit. A detailed Debye model analysis including the scattering of the Umklapp process, grain boundary, and point defects could well predict the variation of thermal conductivity for both MnTe$_{1-x}$Se$_x$ and Na$_{0.01}$Mn$_{0.99}$Te$_{0.92}$Se$_{0.08}$. Due to the contribution of point defect scattering, high *ZT* values of 0.84 and 1.03 were realized in MnTe$_{0.92}$Se$_{0.08}$ and Na$_{0.01}$Mn$_{0.99}$Te$_{0.92}$Se$_{0.08}$, respectively. An enhanced *ZT*$_{ave}$ of 0.52 and a high calculated efficiency of more than 9% also indicate the significant role of point defects and promising application of manganese telluride.

■ ASSOCIATED CONTENT

Ⓢ Supporting Information

The Supporting Information is available free of charge on the ACS Publications website at DOI: 10.1021/acsami.9b10207.

Calculation details of Debye temperature and total relaxation time, parameters for thermal transport modeling; density of synthesized samples; XRD pattern of Se-alloyed and Na-doped MnTe; SEM image on the polished surface of $MnTe_{0.92}Se_{0.08}$ and element distribution; EDS mapping on the TEM image; hole carrier concentrations of $MnTe_{0.92}Se_{0.08}$ and $Na_{0.01}Mn_{0.99}Te_{0.92}Se_{0.08}$; simple schematic illustration of the changes of band gap; temperature-dependent lattice thermal conductivity of $MnTe_{1-x}Se_x$; temperature-dependent thermal conductivity of Se-alloyed and Na-doped MnTe; temperature-dependent lattice thermal conductivity of Se-alloyed and Na-doped MnTe; repeat measurement of Se-alloyed sample and $Na_{0.01}Mn_{0.99}Te_{0.92}Se_{0.08}$; cycle measurement of ZEM-2 of Se-alloyed sample; DSC−TG curves of $MnTe_{0.92}Se_{0.08}$ (PDF)

■ AUTHOR INFORMATION

Corresponding Author

*E-mail: jingfeng@mail.tsinghua.edu.cn.

ORCID Ⓘ

Yuzuru Miyazaki: 0000-0002-3178-5838

Jing-Feng Li: 0000-0002-0185-0512

Notes

The authors declare no competing financial interest.

■ REFERENCES

(1) Bell, L. E. Cooling, Heating, Generating Power, and Recovering Waste Heat with Thermoelectric Systems. *Science* **2008**, *321*, 1457−1461.

(2) Wei, T.-R.; Guan, M.; Yu, J.; Zhu, T.; Chen, L.; Shi, X. How to Measure Thermoelectric Properties Reliably. *Joule* **2018**, *2*, 2183−2188.

(3) Li, J.-F.; Liu, W.-S.; Zhao, L.-D.; Zhou, M. High-Performance Nanostructured Thermoelectric Materials. *NPG Asia Mater.* **2010**, *2*, 152−158.

(4) Zhang, X.; Zhao, L.-D. Thermoelectric Materials: Energy Conversion Between Heat and Electricity. *J. Materiomics* **2015**, *1*, 92−105.

(5) Zhu, T.; Liu, Y.; Fu, C.; Heremans, J. P.; Snyder, J. G.; Zhao, X. Compromise and Synergy in High-Efficiency Thermoelectric Materials. *Adv. Mater.* **2017**, *29*, No. 1605884.

(6) Snyder, G. J.; Toberer, E. S. Complex Thermoelectric Materials. *Nat. Mater.* **2008**, *7*, 105−114.

(7) Mao, J.; Liu, Z. H.; Zhou, J. W.; Zhu, H. T.; Zhang, Q.; Chen, G.; Ren, Z. F. Advances in Thermoelectrics. *Adv. Phys.* **2018**, *67*, 69−147.

(8) Zhao, L.-D.; Tan, G.; Hao, S.; He, J.; Pei, Y.; Chi, H.; Wang, H.; Gong, S.; Xu, H.; Dravid, V. P.; Uher, C.; Snyder, G. J.; Wolverton, C.; Kanatzidis, M. G. Ultrahigh Power Factor and Thermoelectric Performance in Hole-Doped Single-Crystal SnSe. *Science* **2016**, *351*, 141−144.

(9) Pei, Y.; Shi, X.; LaLonde, A.; Wang, H.; Chen, L.; Snyder, G. J. Convergence of Electronic Bands for High Performance Bulk Thermoelectrics. *Nature* **2011**, *473*, 66−69.

(10) Li, J.; Li, W.; Bu, Z.; Wang, X.; Gao, B.; Xiong, F.; Chen, Y.; Pei, Y. Thermoelectric Transport Properties of $Cd_xBi_yGe_{1-x-y}Te$ Alloys. *ACS Appl. Mater. Interfaces* **2018**, *10*, 39904−39911.

(11) Fu, C.; Liu, Y.; Zhao, X.; Zhu, T. Are Solid Solutions Better in FeNbSb-Based Thermoelectrics? *Adv. Electron. Mater.* **2016**, *2*, No. 1600394.

(12) Wu, Y.; Chen, Z.; Nan, P.; Xiong, F.; Lin, S.; Zhang, X.; Chen, Y.; Chen, L.; Ge, B.; Pei, Y. Lattice Strain Advances Thermoelectrics. *Joule* **2019**, *3*, 1276−1288.

(13) Kim, S. I.; Lee, K. H.; Mun, H. A.; Kim, H. S.; Hwang, S. W.; Roh, J. W.; Yang, D. J.; Shin, W. H.; Li, X. S.; Lee, Y. H.; Snyder, G. J.; Kim, S. W. Dense Dislocation Arrays Embedded in Grain Boundaries for High-Performance Bulk Thermoelectrics. *Science* **2015**, *348*, 109−114.

(14) Pan, Y.; Aydemir, U.; Grovogui, J. A.; Witting, I. T.; Hanus, R.; Xu, Y.; Wu, J.; Wu, C.-F.; Sun, F.-H.; Zhuang, H.-L.; Dong, J.-F.; Li, J.-F.; Dravid, V. P.; Snyder, G. J. Melt-Centrifuged $(Bi,Sb)_2Te_3$: Engineering Microstructure toward High Thermoelectric Efficiency. *Adv. Mater.* **2018**, *30*, No. 1802016.

(15) Poudel, B.; Hao, Q.; Ma, Y.; Lan, Y. C.; Minnich, A.; Yu, B.; Yan, X. A.; Wang, D. Z.; Muto, A.; Vashaee, D.; Chen, X. Y.; Liu, J. M.; Dresselhaus, M. S.; Chen, G.; Ren, Z. F. High-Thermoelectric Performance of Nanostructured Bismuth Antimony Telluride Bulk Alloys. *Science* **2008**, *320*, 634−638.

(16) Yamini, S. A.; Wang, H.; Ginting, D.; Mitchell, D. R.; Dou, S. X.; Snyder, G. J. Thermoelectric Performance of N-Type $(PbTe)_{0.75}(PbS)_{0.15}(PbSe)_{0.1}$ Composites. *ACS Appl. Mater. Interfaces* **2014**, *6*, 11476−11483.

(17) Zhang, X.; Wang, D.; Wu, H.; Yin, M.; Pei, Y.; Gong, S.; Huang, L.; Pennycook, S. J.; He, J.; Zhao, L.-D. Simultaneously Enhancing the Power Factor and Reducing the Thermal Conductivity of SnTe via Introducing its Analogues. *Energy, Environ. Sci.* **2017**, *10*, 2420−2431.

(18) Sandratskii, L.; Egorov, R.; Berdyshev, A. Energy Band Structure and Electronic Properties of NiAs Type Compounds. II. Antiferromagnetic Manganese Telluride. *Phys. Status Solidi B* **1981**, *104*, 103−107.

(19) Kim, B.; Kim, I.; Min, B.-k.; Oh, M.; Park, S.; Lee, H. Thermoelectric Properties of Non-Stoichiometric MnTe compounds. *Electron. Mater. Lett.* **2013**, *9*, 477−480.

(20) Dong, J.; Wu, C.-F.; Pei, J.; Sun, F.-H.; Pan, Y.; Zhang, B.-P.; Tang, H.; Li, J.-F. Lead-Free MnTe Mid-Temperature Thermoelectric Materials: Facile Synthesis, P-Type Doping and Transport Properties. *J. Mater. Chem. C* **2018**, *6*, 4265−4272.

(21) She, X.; Su, X.; Xie, H.; Fu, J.; Yan, Y.; Liu, W.; Poudeu Poudeu, P. F.; Tang, X. Ultrafast Synthesis and Thermoelectric Properties of $Mn_{1+x}Te$ Compounds. *ACS Appl. Mater. Interfaces* **2018**, *10*, 25519−25528.

(22) Xin, J.; Yang, J.; Jiang, Q.; Li, S.; Basit, A.; Hu, H.; Long, Q.; Li, S.; Li, X. Reinforced Bond Covalency and Multiscale Hierarchical Architecture to High Performance Eco-Friendly MnTe-based Thermoelectric Materials. *Nano Energy* **2019**, *57*, 703−710.

(23) Ren, Y.; Yang, J.; Jiang, Q.; Zhang, D.; Zhou, Z.; Li, X.; Xin, J.; He, X. Synergistic Effect by Na Doping and S Substitution for High Thermoelectric Performance of P-Type MnTe. *J. Mater. Chem. C* **2017**, *5*, 5076−5082.

(24) Ren, Y.; Jiang, Q.; Yang, J.; Luo, Y.; Zhang, D.; Cheng, Y.; Zhou, Z. Enhanced Thermoelectric Performance of MnTe via Cu Doping with Optimized Carrier Concentration. *J. Materiomics* **2016**, *2*, 172−178.

(25) Xu, Y.; Li, W.; Wang, C.; Li, J.; Chen, Z.; Lin, S.; Chen, Y.; Pei, Y. Performance Optimization and Single Parabolic Band Behavior of Thermoelectric MnTe. *J. Mater. Chem. A* **2017**, *5*, 19143−19150.

(26) Biswas, K.; He, J.; Blum, I. D.; Wu, C. I.; Hogan, T. P.; Seidman, D. N.; Dravid, V. P.; Kanatzidis, M. G. High-Performance

Bulk Thermoelectrics with All-Scale Hierarchical Architectures. *Nature* **2012**, *489*, 414−418.

(27) Chen, Z.; Zhang, X.; Pei, Y. Manipulation of Phonon Transport in Thermoelectrics. *Adv. Mater.* **2018**, *30*, No. 1705617.

(28) Chen, Z.; Ge, B.; Li, W.; Lin, S.; Shen, J.; Chang, Y.; Hanus, R.; Snyder, G. J.; Pei, Y. Vacancy-Induced Dislocations within Grains for High-Performance PbSe Thermoelectrics. *Nat. Commun.* **2017**, *8*, No. 13828.

(29) Xie, W. J.; Populoh, S.; Galazka, K.; Xiao, X. X.; Sagarna, L.; Liu, Y. F.; Trottmann, M.; He, J.; Weidenkaff, A. Thermoelectric Study of Crossroads Material MnTe via Sulfur Doping. *J. Appl. Phys.* **2014**, *115*, 103707−103714.

(30) Shannon, R. D.; Prewitt, C. T. Effective Ionic Radii in Oxides and Fluorides. *Acta Crystallogr., Sect. B: Struct. Crystallogr. Cryst. Chem.* **1969**, *25*, 925−946.

(31) Youn, S. J.; Min, B. I.; Freeman, A. J. Crossroads Electronic Structure of MnS, MnSe, and MnTe. *Phys. Status Solidi B* **2004**, *241*, 1411−1414.

(32) Tit, N.; Obaidat, I. M.; Alawadhi, H. Origins of Bandgap bowing in Compound-Semiconductor Common-Cation Ternary Alloys. *J. Phys.: Condens. Matter* **2009**, *21*, No. 075802.

(33) Cahill, D. G.; Watson, S. K.; Pohl, R. O. Lower Limit to the Thermal Conductivity of Disordered Crystals. *Phys. Rev. B* **1992**, *46*, No. 6131.

(34) Schlichting, K. W.; Padture, N. P.; Klemens, P. G. Thermal conductivity of Dense and Porous Vttria-Stabilized Zirconia. *J. Mater. Sci.* **2001**, *36*, 3003−3010.

(35) Callaway, J.; von Baeyer, H. C. Effect of Point Imperfections on Lattice Thermal Conductivity. *Phys. Rev.* **1960**, *120*, No. 1149.

(36) Wei, T.-R.; Wu, C.-F.; Zhang, X.; Tan, Q.; Sun, L.; Pan, Y.; Li, J.-F. Thermoelectric Transport Properties of Pristine and Na-Doped $SnSe_{1-x}Te_x$ Polycrystals. *Phys. Chem. Chem. Phys.* **2015**, *17*, 30102−30109.

(37) Gong, B.; Li, Y.; Liu, F.; Zhu, J.; Wang, X.; Ao, W.; Zhang, C.; Li, J.; Xie, H.; Zhu, T. Continuously Enhanced Structural Disorder to Suppress the Lattice Thermal Conductivity of ZrNiSn-Based Half-Heusler Alloys by Multielement and Multisite Alloying with Very Low Hf Content. *ACS Appl. Mater. Interfaces* **2019**, *11*, 13397−13404.

(38) Saparamadu, U.; Li, C.; He, R.; Zhu, H.; Ren, Z.; Mao, J.; Song, S.; Sun, J.; Chen, S.; Zhang, Q.; Nielsch, K.; Broido, D.; Ren, Z. Improved Thermoelectric Performance of Tellurium by Alloying with a Small Concentration of Selenium to Decrease Lattice Thermal Conductivity. *ACS Appl. Mater. Interfaces* **2019**, *11*, 511−516.